147 (2023) 213341

Contents lists available at ScienceDirect

Biomaterials Advances

journal homepage: www.journals.elsevier.com/materials-science-and-engineering-c

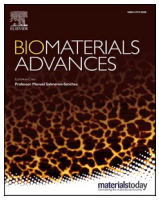

Size and environment: The effect of phonon localization on micro-Brillouin imaging

A.A. Passeri [a], A. Di Michele [a], I. Neri [a], F. Cottone [a], D. Fioretto [a,b], M. Mattarelli [a,*,1], S. Caponi [c,*,1]

[a] Dipartimento di Fisica e Geologia, Università di Perugia, Via A. Pascoli, I-06100 Perugia, Italy
[b] CEMIN, Centre of Excellence on Nanostructured Innovative Materials, University of Perugia, Via Elce di Sotto 8, 06123 Perugia, Italy
[c] Istituto Officina dei Materiali, National Research Council (IOM-CNR), Unit of Perugia, c/o Department of Physics and Geology, University of Perugia, Via A. Pascoli, I-06123 Perugia, Italy

ARTICLE INFO

Keywords:
Brillouin spectroscopy
Micro-mechanical characterization
Thin films
Nanosized materials

ABSTRACT

Specifically designed samples have been analyzed to test the ability of Brillouin spectroscopy to provide reliable mechanical characterization of micro and nano-objects. The selected samples are polymeric films, whose transversal sizes from hundreds of nano- to some micro-meters cover the entire range of length-scales relevant in Brillouin scattering process. The experimental data highlight how, the size of the extended collective oscillation (acoustic phonons, in brief) is the lowest spatial resolution reachable in Brillouin mechanical characterization. Conversely, in the limit condition of phonon confinement, the technique provides the mechanical properties of nano-objects whose characteristic size is comparable with the phonon wavelength (~300 nm). Investigating acoustically heterogeneous materials, both size of heterogeneity and acoustic mismatch between adjacent regions are shown to be relevant in shaping the Brillouin response. In particular, a transition from a confined to a non-confined condition is obtained modulating the acoustic mismatch between the micro-objects and their local environment. The provided results and the derived analytic models for the data analysis will guide the interpretation of Brillouin spectra acquired in complex nano-structured samples such as cells, tissues or biomimetic materials. Our analysis can therefore generate new insights to tackle fundamental problems in mechanobiology or to characterize new bioengineered materials.

1. Introduction

The characterization of the mechanical properties at micro or sub-micrometric length scale is of extreme interest in fundamental research as well as in a large variety of applications ranging from microfabrication [1] through tissue engineering [2] to cell biology [3]. The great translational interest to obtain reliable elastic moduli of micro-objects forced the scientific community to develop new cutting-edge technologies able to perform mechanical tests on such a challenging spatial resolution. In this framework, Brillouin microscopy (BM) is gaining ground: it probes the mechanical properties in non-contact way exploiting the light-matter interaction. It is based on the measure of the frequency shift occurring when a monochromatic beam interacts with the spontaneous acoustic modes present in the materials. The first theoretical prediction of such process was made just one century ago by Leon Brillouin [4], the physicist whose name the technique takes, and, since its first experimental verification [5] in 1930, the great potentiality of the technique has been immediately perceived. The time has proved this expectation right. Nowadays Brillouin spectroscopy is widely used in material science for the characterization of homogeneous and nano-structured materials [6–11] and, in recent years, it extended its applications to the unexpected frontiers of life science and bio-medicine [12–16]. In these frameworks, the use of non-contact methods able to provide high-resolution 3D elastography maps without requiring any physical probe contacting the sample is of extreme interest. The ability of BM is recently proved in a plethora of applications: in developmental biology to study the embryonic formation or the tissue regeneration [17–21], in bio-medicine to detect the onset of pathologies [22–24], in cell biology to providing new methods for cell phenotyping [25,26] and to analyze the nuclear mechanics inside intact cells [27], in

* Corresponding authors.
E-mail addresses: maurizio.mattarelli@unipg.it (M. Mattarelli), silvia.caponi@cnr.it (S. Caponi).
[1] These authors contributed equally to the work.

https://doi.org/10.1016/j.bioadv.2023.213341
Received 20 September 2022; Received in revised form 19 January 2023; Accepted 10 February 2023
Available online 13 February 2023

bioengineering to characterize biomimetic materials [28] with tunable mechanical properties [29] or to analyze the link between the tissue microstructures and its micro-mechanics [30–32]. Moreover, the development of innovative configurations has made it possible to push the technology to study in depth turbid materials [33] or to highly enhance the acquisition speed [34–36].

In particular, the analysis of the heterogeneous biological samples motivated the development of innovative Brillouin microscopes able to produce maps of the elastic properties. Operatively, in this microscope a laser shines a spot on a samples and (a part of) the collected scattered light changes its frequency depending on the mechanical properties of the sample. The resulting mechanical maps are then correlated with bright field images or to complementary imaging technologies [37–41]. However, such correlations are not straightforward because the Brillouin measurement is based on the interplay between the optical field of the incident and scattered photons and the acoustic field of the thermally activated collective oscillations (the so-called acoustic phonons) [42]. While the characteristics of the optical field depend on the optical elements chosen in the microscope, the acoustic phonons are strictly sample dependent [42,43]: on one hand, this guarantees that it is possible to achieve information on a given material characterizing its phonons, and on the other hand, this imposes that the phonons properties guide the technique response. This implies that: i) depending on the direction and polarization of the photons, different phonons will be involved in the scattering process with different wavelength and frequencies. Moreover, the phonons direction dictates the elements of the material elastic tensor which are probed. ii) The actual spatial resolution of Brillouin images is not only driven by the size of the focus of the laser beam but also, by the properties of the acoustic phonons [42,43].

In practice, this interplay is often neglected and the resolution of the optical microscope is confused with the actual spatial resolution of the Brillouin mechanical images, while the spectrum is analyzed in the continuum approximation obtaining from the Brillouin frequency shift, f_B, the sound velocity, v, through the exchanged wavevector of the scattering process, q: f_B, $=vq / 2\pi$. In turn v is related to the longitudinal elastic modulus, M, $M = v^2\rho$ with ρ being the density. This approach can be effective but it presents limits when the features of the sample microstructure are comparable with the characteristic lengths of the Brillouin process (wavelength and extension of the acoustic phonons).

To provide rules to guide the analysis of heterogeneous biological samples and to appreciate the potential of Brillouin imaging, we designed dedicated experiments in order to thoroughly analyze the relevant length scales that play a role in Brillouin spectroscopy. In particular, we analyzed polymeric thin films of variable thickness deposited on a silicon substrate (supported thin film). Their transversal dimension, spanning from nano to micro length scale, covers all the relevant sizes entering in the Brillouin scattering process and mimics the characteristic size of cellular and tissues structures such as organelles and collagen bundles. Moreover, to investigate how the Brillouin response of nano/micrometric objects is modified by the mechanical properties of their environment, each sample is investigated modifying the surrounding media so to reproduce, in a controlled way, the most commons conditions occurring in heterogeneous biological matter. In fact, due to their complex heterogeneous structure, the biological samples present a large variety of situations: the acoustic mismatch between their different parts can be quite small - as happens investigating the nucleus and the cytoplasm of living cells (difference in the order of 5 % for the longitudinal sound velocity [26]) – or extremely high – as occurs in the case of soft extracellular matrix inside the mineralized bone structure (difference in the order of 200 % [44]).

To figure out what is i) the expected Brillouin response in the different cases, ii) the lowest size limit for obtaining a reliable mechanical characterization of the sample microstructures and iii) the right function to model the spectra, we performed an extensive analysis on model systems varying the crucial parameters which drive the Brillouin scattering response. With respect to the biological samples, which do not allow to modulate at will neither the characteristic size of their compartments neither the acoustic mismatch between the different biological parts, model systems provide the necessary flexibility to obtain clear results able to guide the interpretation of Brillouin data.

2. Materials and methods

2.1. Sample preparation

Polymeric films were fabricated by spin coating [45]. Poly(methyl methacrylate) PMMA (purchased from Sigma Aldrich MW ~ 8000) was solubilized in chloroformium changing its concentration. In particular, we used solutions where PMMA was 2.3, 3.0, 3.7, 5.0, 7.0, and 13.0 wt% respectively. As illustrated in Fig. 1a, the solutions are deposited on a silicon substrate and the films are produced using the spin coater at 1000 rpm for 1 min. After the deposition, the samples were allowed to dry in air for 24 h in order to remove the residual solvent. The samples are denominated as fxxx with xxx indicating the nominal thickness in nanometer. As confirmed by SEM analysis, by this procedure films with thicknesses ranging from 250 to 4500 nm were produced.

2.2. Morphology and microstructure

For SEM measurements, the samples were metallized with chromium (8 nm) by sputtering (Quorum Q150T ES) and imaged under a Field Emission Gun SEM LEO 1525 (ZEISS, Jena Germany). As an example, Fig. 1b and c present the images of two films section obtained using 50k× magnification. The obtained samples and the thickness measured by SEM are summarized in Table 1.

2.3. Mechanical and chemical characterization

The mechanical and chemical characterization of the samples were performed using the correlative Raman-Brillouin set-up recently build up in the GHOST Lab in Perugia (Italy) [26,40]. A $\lambda = 532$ nm laser beam (Spectra Physics Excelsior) with a power on the sample of 30 mW is used as light source. The incident and the back-scattered light is focalized on the sample and collected by a microscope objective. For this work, we used the UPLSAPO 60XW from Olympus (NA = 1.2). The measurements were performed focusing the laser spot on the silicon surface just below the films. In this condition, we minimized as much as possible the

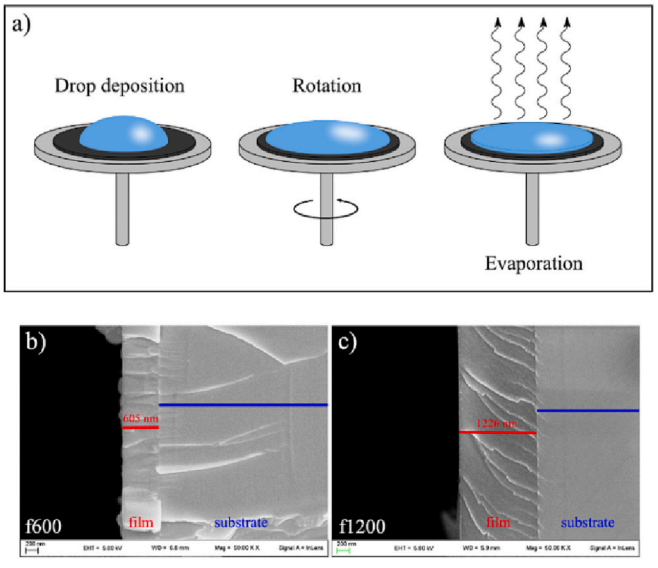

Fig. 1. a) Schematic representation of the spin coating procedure. b) and c) representative SEM images obtained on the sections of the films f600 and f1200 respectively. The measured thickness is reported in the figures.

Table 1
Summary of the structural characterization of the films thickness obtained by SEM together with the fitting parameters obtained by the analysis of Brillouin spectra in air trough Eq. (2). The sound velocity is obtained by $v = 2d\Delta f$. The error in d considers the uncertainty of the refractive index as well as the local variability of the films thickness. The Brillouin data of the sample f4500 are fitted using a damped harmonic oscillator DHO function, where the film thickness, d, does not appear and the sound velocity is related to the peak position, f_B, through the exchanged wavevector, q [14].

		FILM in air		
FILM id	SEM thickness (nm)	Peak width, Γ (GHz)	Thickness, d (nm)	Sound speed v (km/s)
f4500	4500 ± 500	0.57 ± 0.01		2.66 ± 0.01
f1200	1250 ± 40	0.76 ± 0.02	1210 ± 10	2.67 ± 0.02
f900	910 ± 40	0.82 ± 0.02	880 ± 10	2.68 ± 0.02
f600	580 ± 40	0.70 ± 0.02	510 ± 10	2.63 ± 0.02
f500	510 ± 20	0.88 ± 0.02	430 ± 10	2.60 ± 0.02
f300	320 ± 10	1.28 ± 0.06	280 ± 10	2.57 ± 0.03

contribution of the environment maximizing the dimension of the scattering volume filled by the films. In the chosen optical configuration, the z dimension of the scattering volume is about 2 μm, close to the Rayleigh limit (~1.2 μm axially).

The back-scattered light is simultaneously analyzed by a Raman spectrometer (RM- Horiba iHR320 Triax) and a Brillouin TFP-2 HC interferometer so to achieve on the same point of the sample a correlative characterization of its mechanical and chemical properties. In the present study, we analyze the films at normal incidence using a fixed exchanged wave-vector, $q = 4\pi n / \lambda$, being n the refractive index of the investigated material.

3. Results and discussion

3.1. Brillouin spectra of nano-objects: the case of thin films

The Brillouin spectra collected for the whole set of films are reported in Fig. 2c)–d) as separate plots, while the Raman data are superimposed in Fig. 2b). In the chosen scattering geometry, the incident and the scattered beams are orthogonal to the film surface as illustrated in Fig. 2a). Changing the film thickness, the Raman acquisitions present an invariant spectral shape assuring the constant composition and polymer structure. On the contrary, the Brillouin signals significantly changes: reducing the film thickness, Fig. 2c)–d), the spectra evolve, evidencing a transition from a single peak to a multi-peak spectrum.

To explain why Raman and Brillouin spectroscopies give such a different response investigating the same set of samples, it is necessary

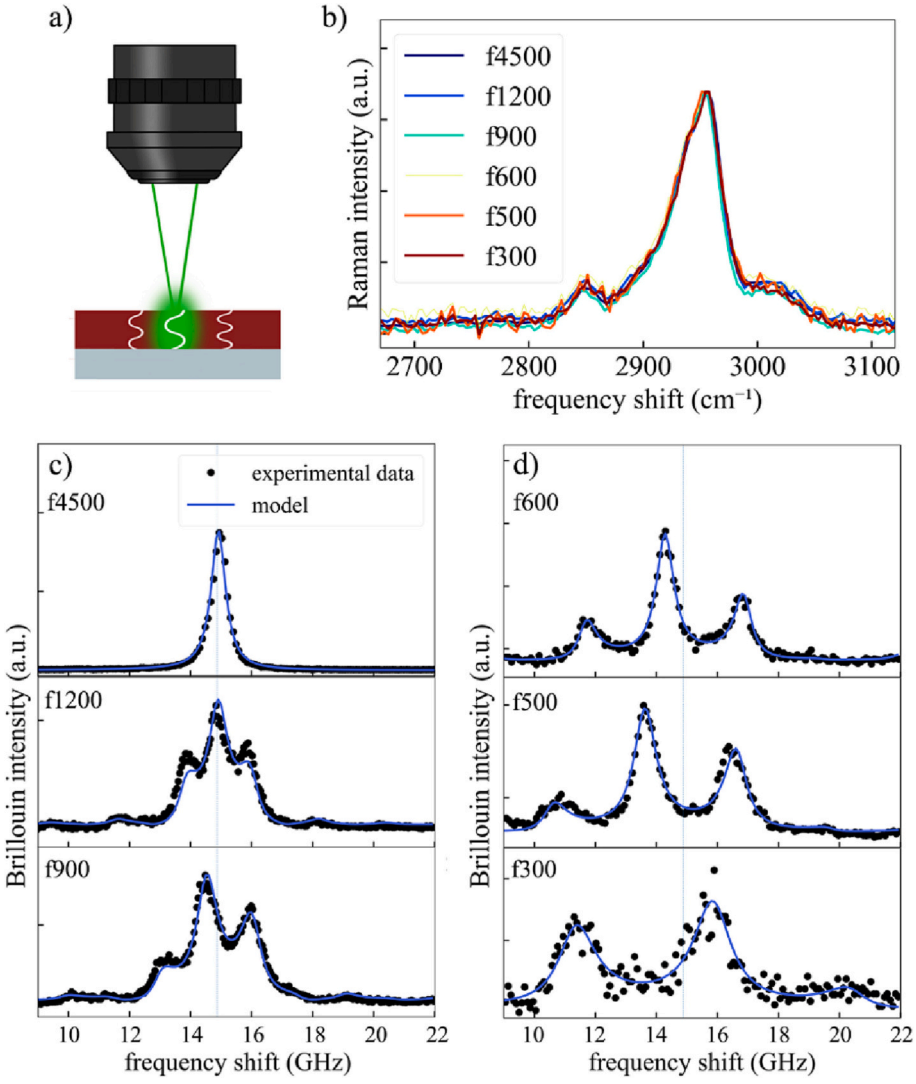

Fig. 2. a) Scheme of the scattering geometry and description of the acoustic standing modes. b) Raman spectra obtained in the set of samples, normalized on the band at ~2900 cm^{-1}. c)–d) Brillouin spectra measured for the whole set of films (full points) compared with the fitting function (lines). The legend reports the film id.

to consider the fundamental difference between the vibrational modes probed by the two techniques. While the former analyzes localized optical modes related to intra- or inter-molecular vibrations, the latter probes the long wavelength acoustic modes which, for their collective nature are extended over a finite space. Therefore, the Raman spectra do not change until the sample reaches size of about 10 nm nanometer [46], while size effect in Brillouin spectra can be observed as soon the relevant sample size is comparable with the extension of the collective acoustic modes [42].

In fact, for a film of a homogeneous lossless material the normal modes along the perpendicular direction to the film surface are characterized by a wavevector, $K_{\perp}$, which assumes discrete values satisfying the boundary conditions. In particular for a film supported on hard substrate, $K_{\perp} = \frac{(2m-1)}{2d}$ where m = 1, 2, 3… and d is the film thickness [47–50] and, as illustrated in Fig. 2a), the allowed acoustic modes present a node at the interface with the substrate and an antinode on the film surface as occurs in organ-pipes [51,52]. Investigating the film at normal incidence, the mode quantization produces in the Brillouin spectrum a series of equally spaced peaks [48], whose distance in frequency, Δf, is related to the sound velocity of the material, v, through the film thickness, i.e. $\Delta f = v / 2d$. As observed and measured as first by J. Sandercock [48] in the early 70s, this comb structure of the acoustic modes in the Brillouin spectra is intensity-modulated by the phase matching condition with the optical scattered field. In particular, the intensity of each $K_{\perp}^{m}$ mode is expressed by a $\mathrm{sinc}^2(x)$ envelope centered around the exchanged wavevector q

$$I_m \propto \frac{sin^2\left[\left(K_{\perp}^{m} - q\right)\frac{d}{2}\right]}{\left[\left(K_{\perp}^{m} - q\right)\frac{d}{2}\right]^2} \quad (1)$$

In this framework, the transition from multi peaks to a single peak spectrum is obtained when the film thickness is such that the frequency separation between peaks is less than the peak halfwidth. This leads to the observation of a single peak centered at frequency $vq / 2\pi$, retrieving the result obtained for the bulk material. In fact, this view is correct only if the medium is lossless, where the peak broadening is due to instrumental resolution with the underlying acoustic modes remaining sharp. If there is friction, not only the peak width is increased, potentially facilitating the peaks merging, but, if the coherence length is less than the film thickness, the boundary conditions no longer have to be met. In this case a continuum of acoustic modes exists in the materials and it contributes to the Brillouin spectrum.

The coherence length of the phonons, l_c, is the dimension of the region in which the density fluctuations that give rise to the Brillouin signal are correlated. It depends on the material and can be estimated from the peak width Γ_B, as $l_c \sim \Lambda f_B / \Gamma_B$ where Λ is the wavelength of the investigated phonons $\Lambda = 2\pi / q$ [42,43].

Indeed, for the thickest film (f4500 in Fig. 2c), the spectral features resemble the usual Brillouin spectrum obtained in bulk materials. The characteristic peak of the longitudinal acoustic mode (LA) appearing in the spectrum at about 15 GHz, corresponds to $v_{PMMA} = 2660 \pm 10$ m/s, while l_c results about 4.5 μm. Conversely, the other films which have thickness below l_c show in the Brillouin spectrum the typical multipeak structure of a system with discrete acoustic modes. To obtain the physical parameters from the experimental data, the data treatment has to take into account the previous theoretical description. The collected spectra, were fitted by the following expression, which considers a single Lorentzian peak of width Γ for each acoustic transversally confined mode with an intensity modulated by the expression (1):

$$I_m(x) = c + I\sum_{m} \frac{\Gamma/2}{(\Gamma/2)^2 + \left(x - \frac{(2m-1)\Delta f}{2}\right)^2} \mathrm{sinc}^2\left(\frac{\pi}{2\Delta f}\left(x - \frac{4\, n\, d\, \Delta f}{\lambda_i}\right)\right) \quad (2)$$

where c and I take into account the slight background and the overall intensity, while λ_i is the wavelength of the incident laser beam (532 nm). In the fitting procedure, c, I, Δf, d and Γ were free parameters, while the value of the refractive index of PMMA film, n, was fixed at n = 1.49, [53] and m ranging from −20 to 20 is chosen for all the investigated films. Note that this fitting function neglects the minor contribution of ripple effect to the scattered intensity [49].

With respect to the previous literature, for the first time, we attempt a complete description of the experimental data acquired on thin films using a unique fitting function to describe the complete spectral shape. In this way it is possible: i) to emphasize how Brillouin spectroscopy is able to provide morphological as well as mechanical properties of a priori unknown nano-sized objects — indeed, as often occurs in the characterization of biological structures, the characteristic size and the mechanical properties of the investigated samples are often unknown; ii) to compare the obtained values for v and d with the expected ones valuating the confidence of the proposed data treatment; iii) to provide the width of the peaks Γ a parameter never obtained until now in the thin film analysis. Fig. 2c)–d) shows the comparison between the fitting functions and the experimental data. The values of the sound speed and the film thicknesses obtained by the fitting process are summarized in Table 1 finding a good agreement with the sound speed expected for the PMMA sample as measured on the thickest film (maximum deviation less than 4 %) and the film thicknesses measured by the SEM characterization (maximum deviation less than 15 %). It is worth to notice that the d values obtained by SEM are always greater than the ones obtained by fitting the Brillouin data. A possible explanation can be sought considering that, while the Brillouin measurements are performed on intact samples, the SEM analysis is performed along the transversal section of the film obtained by cutting the samples. Hence the SEM analysis could be affected by thickness changes occurred after sectioning the sample, when tension stresses originated during the sample preparation process are released. Hence, SEM provides only an approximated value for the thickness in the point investigated by Brillouin/Raman spectroscopy.

On the other hand, the deviation from the expected sound velocity can provide the efficacy of the proposed method, the confidence is very high for the thickest films while it decreases to reach about 4 % decreasing the sample size. The here reported data confirm that Brillouin spectroscopy can provide reliable mechanical characterization in micro and nano-objects even when the sample size is comparable with the wavelength of the investigated phonons (~300 nm). However, the estimation of the mechanical properties on such length scale can be achieved only using the appropriate theoretical model, which has to take into account the confinement of the acoustic modes and the multi-peak structure of the Brillouin spectrum. The use of the continuum model, which relates each peak present in the spectrum to materials with different elastic properties, would lead to an incorrect characterization of the sample.

The analysis of the Brillouin spectra of thin films provides two main results: as first, the exchanged wave-vector, q, does not select the probed phonons, as occurs in bulk materials, rather it determines the scattering efficiency of the different modes. This effect, which is a general feature of Brillouin scattering, is evident only when the sample structure due to the phonon confinement induces a discretization of the modes: it has been already observed investigating the acoustic normal modes in spherical or ellipsoidal microparticles or in thin films investigated in different scattering geometries [7,50,54].

As a second important remark, we found that investigating micro and nanostructured materials, the Brillouin response is deeply dependent on the characteristic size of the sample. As a rule of thumb, when the characteristic sample size, d, is larger than coherence length of the phonons l_c, the sample behave as infinite system and the continuum model can be applied, when $d < l_c$ the phonons suffer the confinement effect induced by the sample micro-structure. In this latter condition, the spectra present the characteristic multi-peak structure which is still linked to the sound velocity but through the sample morphology.

3.2. Micro-environment effect on the mechanical characterization

In the following, we analyze the influence of the environment in the Brillouin characterization of micro-objects. With this aim, the same supported films characterized in the previous section were investigated once immersed in two different materials, water and glycerol, chosen to progressively reduce the mechanical mismatch between the film and the surrounding material ($v_{H2O} = 1500$ m/s, $\rho_{H2O} = 1$ g/cm^3, $v_{gly} = 2800$ m/s $\rho_{gly} = 1.26$ g/cm^3 vs $v_{PMMA} = 2700$ m/s, $\rho_{PMMA} = 1.18$ g/cm^3). The layout of the experimental configuration is reported in the panels a) of Fig. 3 and Fig. 4: the upper surface of the films is in contact with water or glycerol.

The acquisition of the Raman spectra, lets to analyze the chemical composition of the probed point. In fact, the Raman spectra present the linear combination of the signals of the different materials present in the scattering volume, where their relative intensity is weighted by the scattering efficiency and by the volume filling fraction. In particular, the Raman spectra presented in Fig. 3d), shows the two characteristic bands of water and PMMA: the band centered at about 2950 cm^{-1}, assignable to the $-CH_2$ and $-CH_3$ stretching modes of the polymer (red lines), is superimposed to the O—H stretching mode of the surrounding bulk water (blue lines), centered at about 3200 cm^{-1}. In the same way, the Raman band centered at 2950 cm^{-1} in Fig. 4d) is due to the contribution of glycerol (blue lines) and PMMA (red lines), both of them present in the scattering volume. The simultaneous acquisition of Brillouin and Raman spectrum allows us to be certain of observing the same scattering volume in the PMMA film and that any change in the Brillouin spectrum is due to a modification of the properties of the acoustic phonons in the observed volume.

In fact, the behavior of the Brillouin spectra is quite more complex with respect to Raman ones. Fig. 3b) presents the Brillouin spectrum of the f500 film immersed in water, showing the contribution of both the water (peak centered at about 7.5 GHz) and the characteristic features of the film signal growing on the high frequency tail of the water contribution. Just from the raw data, it is possible to notice that, even if well detectable, the film spectrum is drastically modified, so that the signal measured by Brillouin technique cannot be simply explained by a linear combination of the spectra measured for the different materials. As shown in Fig. 3c), where only the high frequency part of the spectra is reported, regardless the sample thickness, the film peaks appeared less defined and the width Γ of the multi-peak structure is drastically increased with respect to the measurements performed in air. For an effective evaluation of this behavior, Eq.2 is used to fit the data once added the signal of the water, separately acquired. The water and the film contributions (red and light blue lines, respectively) together with their sum (blue) are reported in Fig. 3c) and the fit results are reported in Table 2. Comparing the fitting parameters obtained for films in air and in water, Table 1 and Table 2 respectively, it is found that the sound speed and the film thickness are in quite good agreement while the widths of the peaks in the latter condition are almost doubled, evidencing the presence of a further mechanism which contributed to the acoustic dissipation. The large relative error present in the values obtained in the sample f300 deserves a separate discussion. The relative intensity of the film signal is lower and lower decreasing its thickness. In the case of the thinnest film f300 immersed in water, only one peak of the envelope can be clearly recognized in the spectrum. The other peaks are too low and are hidden below the signal of water. In this condition the evaluation of Δf (frequency spacing between the films peaks) is affected by a large error, which is consequently transferred to the values of the film thickness and speed of sound.

Investigating the same set of films once inserted in glycerol the situation is once again different. The multipeak structure in the Brillouin spectra is completely lost (Fig. 4c) and the signal of the bulk glycerol is perturbated by the film presence. The modification induced by the film presence is well detectable in the spectra of the thickest films (f1200 and f900), while it is not easily distinguishable from the noise for the thinner ones (f600–f500–f300).

To highlight the modifications of the film spectral contributions in the three different conditions here investigated, Fig. 5 summarizes the direct comparison of the film signal acquired in air with the ones obtained in different environments, i.e. water and glycerol. Even if the films and hence their mechanical properties are always the same, the Brillouin response is completely different: this result clearly indicates how Brillouin spectra are strongly dependent on the local environment when micro-objects are under investigation.

The origin of such behavior can be explained by differences in the phonon confinement: the high mechanical mismatch present in the first configuration (silica substrate-PMMA film-air) ensures the most effective transversal phonon confinement and the quantized modes responsible of the multipeak structure in the Brillouin spectra appear well separated. Reducing the acoustic mismatch, the phonon confinement progressively decreases. The multipeak structure is still detectable in the case of (silica substrate-PMMA film-water) while reaching the last configuration (silica substrate-PMMA film-glycerol), the mechanical properties of the PMMA and glycerol are so close that there is not any detectable confinement. In this condition, the phonons can actually extend across the PMMA/glycerol interface and the properties that we measure by Brillouin spectroscopy will depend on both materials. In fact, the contribution to the observed spectrum in the glycerol/PMMA of the film is not equal to the spectrum of PMMA. Instead, it represents that change of the acoustic modes near the interface due to the presence of both PMMA and glycerol. Therefore, the final contrast in the Brillouin mechanical imaging is not only related to the visco-elastic properties of the micro-object under investigation, but also to the acoustic mismatch existing between the micro-object and its surrounding material. The data demonstrate how the Brillouin response is not exclusively driven by the mechanical propriety of the materials but, below a certain length scale, also by the sample morphology. The allowed acoustic phononic modes, which are responsible for the Brillouin scattering, depend on the geometry of nano/micro-objects and on their local environment. By interacting with the light, according to the momentum and energy conservation rules, one or more of the pre-existing phononic modes are then made evident in the Brillouin spectrum. This complex process influences the spatial resolution and hence interpretation and data analysis.

3.3. Film as resonant cavity for the acoustic waves

To provide a more quantitative and general description able to drive the future interpretation of Brillouin maps obtained for nanostructured materials, we can schematize the situation considering the film – or the micro-object – as a resonant cavity for the acoustic waves with leaks at the interfaces. The acoustic mismatch between the acoustic impedances ($Z = \rho v$) of the materials at the interfaces defines the amount of the leaks and the efficiency of the energy confinement inside the cavity, i.e. the cavity merit factor. Let's consider the interface between materials namely A and B. The acoustic mismatch can be quantified by the ratio of the acoustic impedances of the two media:

$$\Delta Z_{A-B} = Z_A / Z_B$$

If $\Delta Z_{A\text{-}B}$ is close to 1, there is low acoustic mismatch and the acoustic wave energy is almost entirely transmitted. On the other hand, in case of high acoustic mismatch, the transmission at the interface goes to zero and the acoustic waves are confined inside one medium. The transmission and reflectance coefficients, $T = \frac{4Z_A Z_B}{(Z_A+Z_B)^2}$ and $R = \left(\frac{Z_A-Z_B}{Z_A+Z_B}\right)^2$, define the amount of energy transmitted and reflected through the interface. The values of $\Delta Z_{A\text{-}B}$, T and R for the different couples of materials here investigated, are reported in Table 3.

In the first analyzed case, the acoustic mismatches between the air and the PMMA and between the PMMA and the silica substrate are high enough to guarantee the acoustic confinement inside the film. Modifying

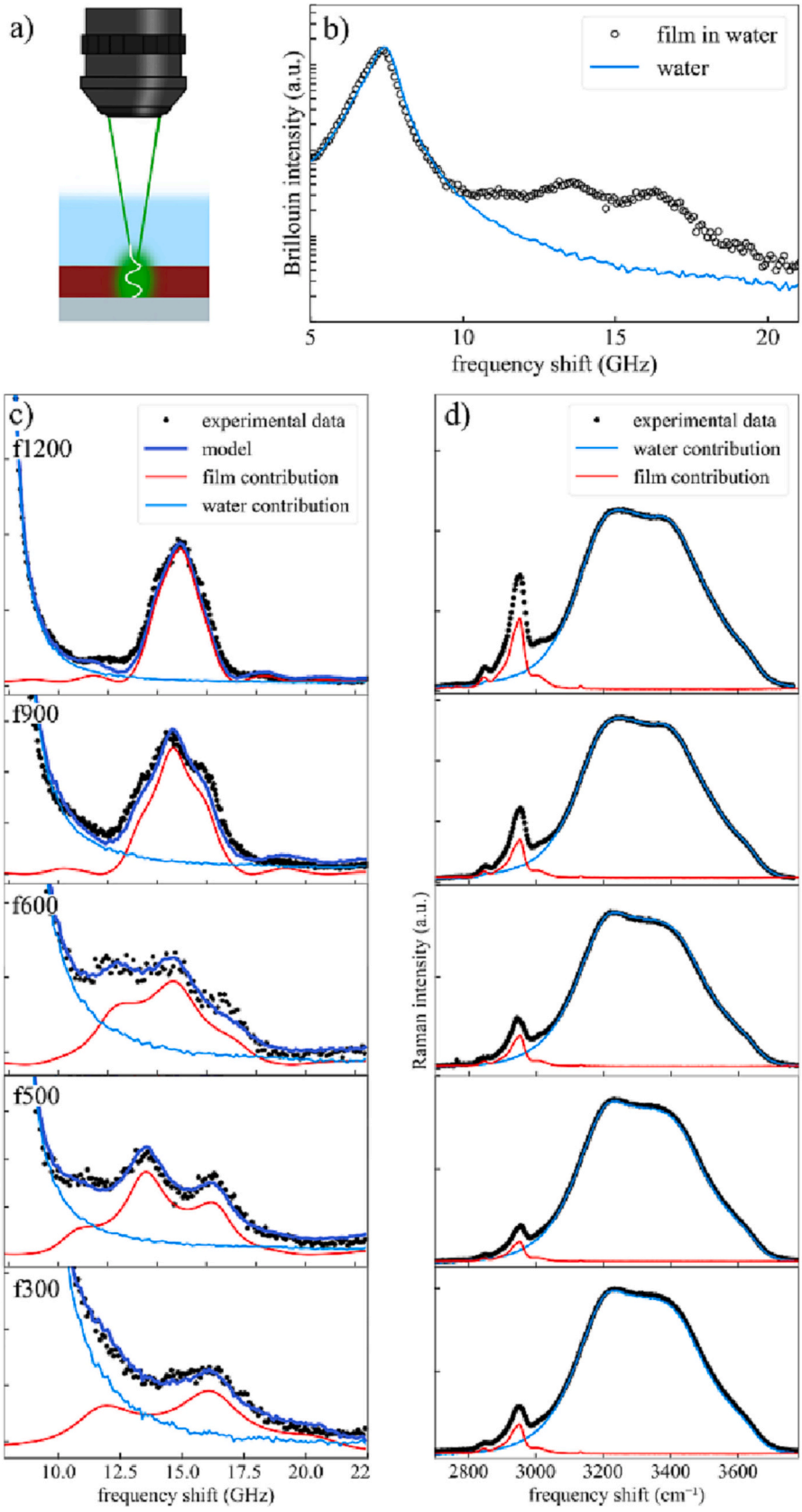

Fig. 3. a) Experimental configuration: the thin film is immersed in water and the microscope objective focalizes and collects the light inside the film. b) Stokes-side of a representative Brillouin spectrum acquired in a film immersed in water (dots) compared with the water spectrum (light blue line). c) High frequency part of the Brillouin spectrum acquired for the indicated films immersed in water. The experimental data (black points) are compared with the fitting function (blue) obtained summing the water contribution (reported in light blue) with the film signal modelled by Eq. 2 where the refractive index of PMMA, n, was fixed at n = 1.49. The different contributions to the fitted spectrum are reported for the film (in red) and for the water. d) High frequency part of the Raman spectrum. Together with the data (black points), the water (light blue) and the film (red) contributions are also highlighted.

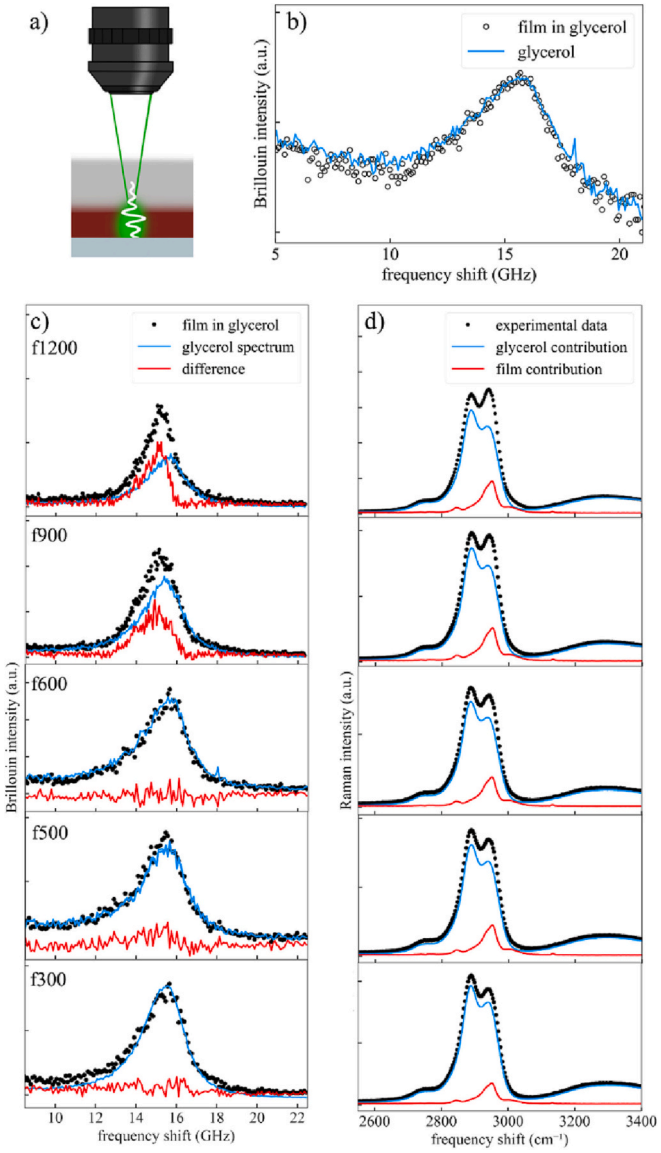

Fig. 4. a) Experimental configuration: the thin film is immersed in glycerol and the microscope objective focalizes and collects the light inside the film. b) Stokes-side of a representative Brillouin spectrum acquired in a film immersed in glycerol (circles) compared with the glycerol spectrum (light blue line). c) Brillouin spectrum acquired for the indicated films immersed in glycerol. The experimental data (black points) are compared with the spectrum of the glycerol (light blue) and their difference due to the film contribution is reported in red. d) High frequency part of the Raman spectrum. Together with the data (black points), the glycerol (light blue) and the film (red) contributions are also highlighted.

Table 2
Fitting parameters obtained by the analysis of Brillouin spectra measured in thin films immersed in water. The error in d considers the uncertainty of the refractive index as well as the local variability of the films thickness.

	FILM in water		
FILM id	Thickness, d (nm)	Peak width Γ (GHz)	Sound speed v (km/s)
f1200	1100 ± 10	1.5 ± 0.2	2.67 ± 0.02
f900	870 ± 10	1.5 ± 0.1	2.66 ± 0.02
f600	480 ± 10	2.30 ± 0.05	2.56 ± 0.05
f500	420 ± 10	2.00 ± 0.02	2.58 ± 0.04
f300	290 ± 10	2.9 ± 0.2	2.7 ± 0.1

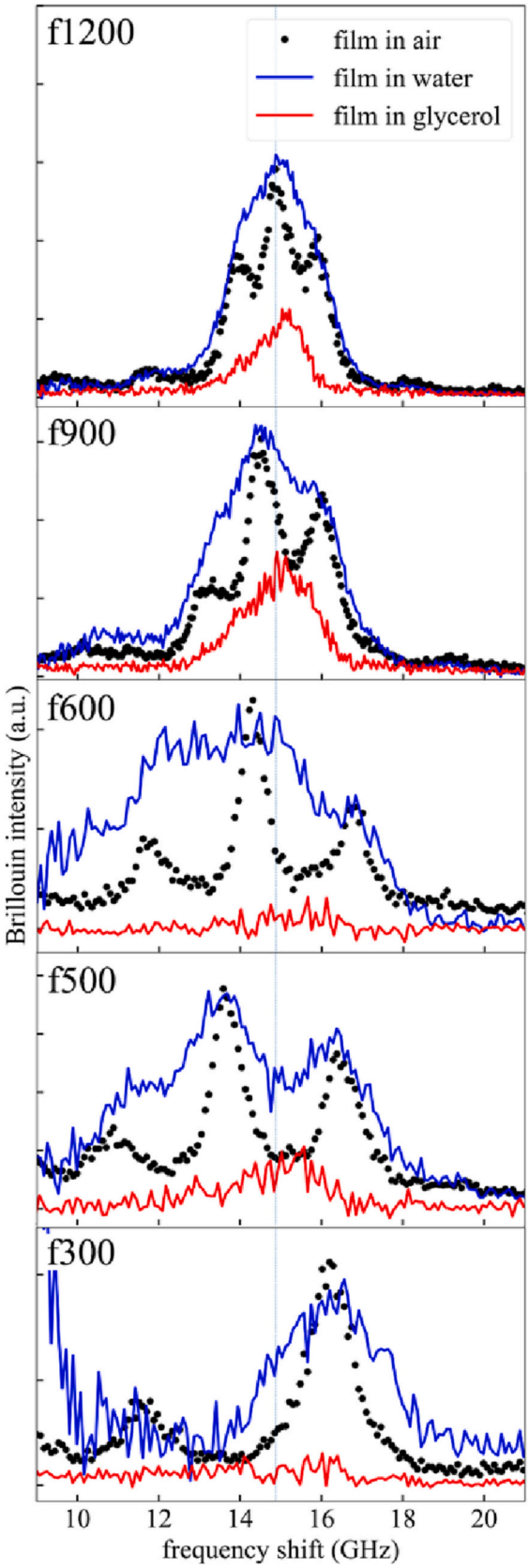

Fig. 5. Comparison of the Brillouin signal measured for the same supported films investigated using three different surrounding materials: air (black lines), water (blue lines) and glycerol (red). The legend report the film name. The vertical line represents the position of Brillouin peak for bulk PMMA.

Table 3
The values of acoustic mismatch, $\Delta Z_{A\text{-}B}$, transmittance, T, and reflectance, R, for the different couples of materials here investigated.

Interface	Acoustic mismatch (ΔZ)	Transmittance	Reflectance
PMMA + air	$8.8 \cdot 10^3$	$5 \cdot 10^{-4}$	0.9995
PMMA + silica	6	0.47	0.53
PMMA + H_2O	2	0.89	0.11
PMMA + glycerol	0.8	0.99	0.01

the upper interface, the acoustic confinement changes. In the case of water, the PMMA-water interface presents an acoustic mismatch of $\Delta Z_{PMMA-water} \sim 2$ corresponding to a transmittance T = 0.89. Here, most of the acoustic wave intensity is transmitted through the interface, but the confined component is high enough to be still probed in the Brillouin spectra. In the case of glycerol, the $\Delta Z_{PMMA-glycerol} \sim 0.8$ leading to a T value close to one, which prevents the acoustic confinement.

Modeling the PMMA film as a resonant cavity, where the acoustic losses are due to the transmissions at the interfaces and following the analogy with a Fabry Perot cavity for the optical modes, the peak broadening can be expressed by [55]:

$$\Gamma_R = -\frac{ln(R_{AB}R_{BC})}{2\pi t_{RT}}$$

where Γ_R is the contribution to the width of the Brillouin peak due to the losses at the interfaces, $t_{RT} = 2d / v$ is the round-trip time, i.e., the time needed for the acoustic wave to travel back and forth along the cavity, while R_{AB} and R_{BC} are the reflectance coefficients at the two film interfaces. In particular, R_{AB} will always be referred to the PMMA-silica substrate, while R_{BC} will be the reflectance coefficient calculate for the PMMA in the three investigated cases, i.e. air, water and glycerol respectively.

It has to be noticed that according to the previous model, the increase of the Brillouin width due to the interfaces, Γ_R, is not constant but it is inversely proportional to the film thickness. To compare the results of our model with the experimental data, we report in Fig. 6, both the fit results and the expected values of our model.

The expected total width, Γ, is obtained summing to the leakage contribution Γ_R the contribution $\Gamma_B = 0.57 \pm 0.01$ GHz, which represents the intrinsic width of the Brillouin peak due to internal friction, as measured in bulk.

The comparison shows good agreement for both water and air as the surrounding material. The scattering of the data is a signal of the presence of other dissipation effects in real films with respect to the ideal case, such as for instance some surface roughness.

In the case of glycerol, the expected width of the peaks (~4.4 GHz) is comparable with the peaks frequency spacing (maximum expected value ~3 GHz). Indeed, it indicates that the leakage of the acoustic energy is so high that it is no longer possible to speak of confined modes.

4. Conclusions

Brillouin microscopy is emerging as a new powerful tool in the characterization of mechanical properties of heterogeneous micro and nano structured materials. For its unique abilities, the technique was applied to a large variety of biological samples where the mechanical properties act as pivotal regulators in their physiological and pathological development.

However, to extend its application fields and to obtain reliable results in the investigation of complex heterogeneous materials, it is important to understand i) what is the expected Brillouin signal for different microscopic geometries and ii) which is the most correct way to extract the mechanical information from the spectrum. To answer these questions, we investigated a well-known polymeric material – PMMA – modulating its characteristic size and the mechanical properties of the surrounding micro-environment. The obtained data highlight how the Brillouin response is not univocally linked to the mechanical properties of the PMMA, but it strongly depends on the confinement of the acoustic phonons. The Brillouin spectrum presents a single peak when a bulk PMMA sample is investigated, while for the micro/submicrometric films, the Brillouin signal has a multipeak spectral shape whose features – peak position and width – are strongly dependent on the local environment and the characteristic size of the sample.

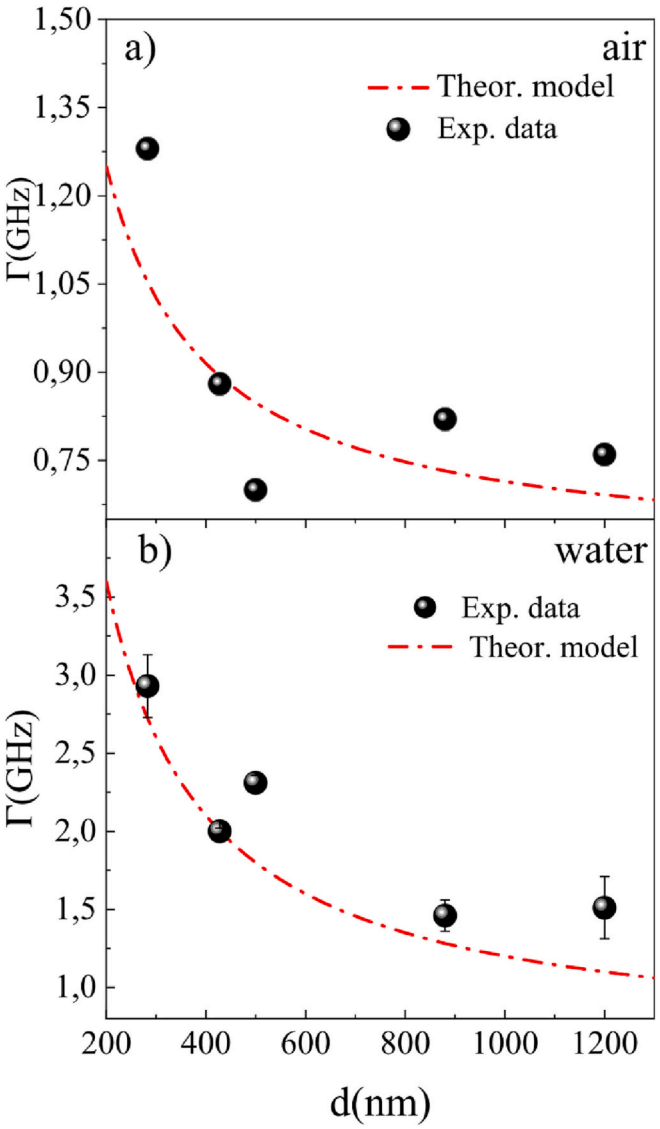

Fig. 6. Comparison between the expected (red dots and line) and the measured (black points) values of the Brillouin width, Γ, as a function of the film size. The data of panel a) refer to the case of confined acoustic waves (film in air). The data of panel b) refer to the case of partial confinement of the acoustic waves (film immersed in water).

The analysis of the films, performed using a newly introduced fitting function, which attempts the complete description of the experimental data, highlights the limit and the potentiality of the technique: to determine the minimum resolvable detail in mechanical images, it is necessary to consider from the fundamental point of view, how the sample microstructure affects the acoustic field. In particular, for large samples, the coherence length of the phonons can be considered the lowest limit reachable in the Brillouin mechanical maps. On the other hand, when the size of the investigated sample is comparable with the wavelength of the investigated phonons and a high acoustic mismatch exists between the sample and the surrounding material, the acoustic

confinement allows to obtain a reliable mechanical characterization on lower length scales. In particular, we demonstrated the possibility to extract the mechanical properties of nanoobjects, whose width d is comparable with the wavelength of the phonons (300 nm) i.e. much smaller than the coherence length of the phonons in bulk PMMA, albeit changing the theoretical model needed for its determination. However, this result is no longer achievable when a low acoustic mismatch exists between the sample and the surrounding material. In this case, the acoustic phonons extend across the interface between the sample and the local environment, hindering a reliable mechanical characterization of the different micro-structures present in the scattering volume. It is important to underline that this effect is independent on the frequency resolution of the Brillouin spectrometer: it is an intrinsic property of the phonons of the studied system.

The obtained results give fundamental insights for guiding the Brillouin analysis in every sample composed by different structures, such as cells or tissues: investigating heterogeneous materials at submicrometric scale, it is necessary to evaluate the acoustic mismatch between the different parts of the samples to understand when it is theoretically justified that different contributions appear in the spectra and vice versa when the presence of a single peak, possibly modified by the surrounding material, is to be expected. Furthermore, these results provide some caveats to the application of spectral decomposition in the analysis of complex Brillouin spectra, as it is often carried out in Raman spectroscopy. In fact, according to the continuum model, in order to have independent Brillouin peaks in the same spectrum either the materials should have high mechanical mismatch [31] or the size of the different materials within the scattering volume should be greater than the coherence length of the phonons so that the interface contribution can be neglected [26]. Smaller features observed in Brillouin maps should be considered as effective signals of mechanical contrast at (sub-) microscale, but without assigning high significance to the absolute values of the measured parameters. In fact, overcoming this limit is possible only if, as for some techniques of optical super resolution such as SMLM [56], the features (shape, for instance) of the elastic heterogeneities that give rise to the acoustic perturbation are known a priori. In this case a deconvolution procedure can lead to a resolution even higher than the phonon wavelength [57].

This analysis has a general relevance, and it can help to guide the future interpretation of the Brillouin elastography maps achievable in complex materials. Only the correct evaluation of the Brillouin maps can provide new and accurate insight linking the mechanical properties to the dynamics and the interactions occurring in living systems, or can drive the development of new biomaterials characterized by designed structures with certain mechanical properties at micro or submicrometric length scales.

CRediT authorship contribution statement

A.A. Passeri: Validation, Software, Formal analysis, Investigation.
A. Di Michele: Resources.
F. Cottone: Resources.
I. Neri: Software.
D. Fioretto: Supervision, Funding acquisition.
S. Caponi e M. Mattarelli: Conceptualization, Software, Project, administration Supervision, Methodology, Writing – review & editing.
All authors read and approved final version of the manuscript.

Declaration of competing interest

The authors declare that they have no known competing financial interests or personal relationships that could have appeared to influence the work reported in this paper.

Data availability

Data will be made available on request.

Acknowledgment

This work has been partially funded by the European Union - NextGenerationEU under the Italian Ministry of University and Research (MUR) National Innovation Ecosystem grant ECS00000041 - VITALITY. We acknowledge Università degli Studi di Perugia, CNR and MUR for support within the project Vitality. DF and MM also acknowledge the CARIT -Fondazione Cassa di Risparmio di Terni e Narni- for support within the project FCTR21UNIPG.

References

[1] V.T. Srikar, S.M. Spearing, A critical review of microscale mechanical testing methods used in the design of microelectromechanical systems, Exp. Mech. 43 (2003) 238–247, https://doi.org/10.1007/BF02410522.
[2] S.J. Hollister, Porous scaffold design for tissue engineering, Nat. Mater. 4 (2005) 518–524, https://doi.org/10.1038/nmat1421.
[3] P.H. Wu, A. Asnacios, W.C. Chen, M.E. Dokukin, B.L. Doss, P. Durand-Smet, A. Ekpenyong, J. Guck, P.A. Janmey, J.S.H. Lee, N.M. Moore, A. Ott, Y.C. Poh, R. Ros, M. Sander, I. Sokolov, J.R. Staunton, N. Wang, G. Whyte, D. Wirtz, D.R. ben Aroush, N.V. Guz, A comparison of methods to assess cell mechanical properties, Nat. Methods 15 (2018) 491–498, https://doi.org/10.1038/s41592-018-0015-1.
[4] L. Brillouin, Diffusion de la lumière et des rayonnes X par un corps transparent homogéne; influence del'agitation thermique, Ann. Phys. 9 (1922) 88–122, https://doi.org/10.1051/anphys/192209170088.
[5] E. Gross, Change of wave-length of light due to elastic heat waves at scattering in liquids, Nature 126 (1930) 201–202, https://doi.org/10.1038/126201a0.
[6] W. Cheng, J. Wang, U. Jonas, G. Fytas, N. Stefanou, Observation and tuning of hypersonic bandgaps in colloidal crystals, Nat. Mater. 5 (2006) 830–836, https://doi.org/10.1038/nmat1727.
[7] T. Still, M. Mattarelli, D. Kiefer, G. Fytas, M. Montagna, Eigenvibrations of submicrometer colloidal spheres, J. Phys. Chem. Lett. 1 (2010) 2440–2444, https://doi.org/10.1021/jz100774b.
[8] C.E. Bottani, D. Fioretto, Brillouin scattering of phonons in complex materials, Adv Phys X. 3 (2018) 1467281, https://doi.org/10.1080/23746149.2018.1467281.
[9] F. Kargar, A.A. Balandin, Advances in Brillouin-Mandelstam light-scattering spectroscopy, Nat. Photonics 15 (2021) 720–731, https://doi.org/10.1038/s41566-021-00836-5.
[10] D. Schneider, N. Gomopoulos, C.Y. Koh, P. Papadopoulos, F. Kremer, E.L. Thomas, G. Fytas, Nonlinear control of high-frequency phonons in spider silk, Nat. Mater. 15 (2016) 1079–1083, https://doi.org/10.1038/nmat4697.
[11] K. Rolle, H.J. Butt, G. Fytas, Flash Brillouin scattering: a confocal technique for measuring glass transitions at high scan rates, ACS Photon. 8 (2021) 531–539, https://doi.org/10.1021/acsphotonics.0c01533.
[12] R. Prevedel, A. Diz-Muñoz, G. Ruocco, G. Antonacci, Brillouin microscopy - a revolutionary tool for mechanobiology? Nat. Methods 16 (2019) 969–977.
[13] Z. Meng, A.J. Traverso, C.W. Ballmann, M. Troyanova-Wood, V.V. Yakovlev, Seeing cells in a new light: a renaissance of Brillouin spectroscopy, Adv. Opt. Photon. 8 (2016) 300–327, https://doi.org/10.1364/AOP.8.000300.
[14] F. Palombo, D. Fioretto, Brillouin light scattering: applications in biomedical sciences, Chem. Rev. 119 (2019) 7833–7847, https://doi.org/10.1021/acs.chemrev.9b00019.
[15] S. Caponi, A. Passeri, G. Capponi, D. Fioretto, M. Vassalli, M. Mattarelli, Non-contact elastography methods in mechanobiology: a point of view, Eur. Biophys. J. 51 (2022) 99–104, https://doi.org/10.1007/s00249-021-01567-9.
[16] E. Frittoli, A. Palamidessi, F. Iannelli, F. Zanardi, S. Villa, L. Barzaghi, H. Abdo, V. Cancila, M. Pagani, C. Malinverno, D. Bhattacharya, F. Pisati, W. Yu, V. Galimberti, G. Bonizzi, E. Martini, A.A. Mironov, U. Gioia, F. Ascione, Q. Li, K. Havas, S. Magni, Z. Lavagnino, F.A. Pennacchio, P. Maiuri, S. Caponi, M. Mattarelli, S. Martino, F. d'Adda di Fagagna, C. Rossi, M. Lucioni, R. Tancredi, P. Pedrazzoli, A. Vecchione, C. Petrini, F. Ferrari, C. Lanzuolo, G. Bertalot, G. Nader, M. Foiani, M. Piel, R. Cerbino, F. Giavazzi, C. Tripodo, G. Scita, G. V. Beznoussenko, G. della Chiara, Tissue fluidification promotes a cGAS–STING cytosolic DNA response in invasive breast cancer, Nat Mater. (2022), https://doi.org/10.1038/s41563-022-01431-x.
[17] L. Bacete, J. Schulz, T. Engelsdorf, Z. Bartosova, L. Vaahtera, G. Yan, J.M. Gerhold, T. Tichá, C. Øvstebø, N. Gigli-Bisceglia, S. Johannessen-Starheim, J. Margueritat, H. Kollist, T. Dehoux, S.A.M. McAdam, T. Hamann, THESEUS1 modulates cell wall stiffness and abscisic acid production in Arabidopsis thaliana, Proceedings of the National Academy of Sciences. 119 (2022), https://doi.org/10.1073/pnas.2119258119.
[18] R. Schlüßler, S. Möllmert, S. Abuhattum, G. Cojoc, P. Müller, K. Kim, C. Möckel, C. Zimmermann, J. Czarske, J. Guck, Mechanical mapping of spinal cord growth and repair in living zebrafish larvae by Brillouin imaging, Biophys. J. 115 (2018) 911–923, https://doi.org/10.1016/j.bpj.2018.07.027.
[19] C. Riquelme-Guzmán, T. Beck, S. Edwards-Jorquera, R. Schlüßler, P. Müller, J. Guck, S. Möllmert, T. Sandoval-Guzmán, In vivo assessment of mechanical

properties during axolotl development and regeneration using confocal Brillouin microscopy, Open Biol. 12 (2022), https://doi.org/10.1098/rsob.220078.
[20] R. Raghunathan, J. Zhang, C. Wu, J. Rippy, M. Singh, et al., Evaluating biomechanical properties of murine embryos using Brillouin microscopy and optical coherence tomography, J. Biomed. Opt. 22 (2017) 1, https://doi.org/10.1117/1.jbo.22.8.086013.
[21] E. Pukhlyakova, A.J. Aman, K. Elsayad, U. Technau, β-Catenin–dependent mechanotransduction dates back to the common ancestor of Cnidaria and Bilateria, Proceedings of the National Academy of Sciences. 115 (2018) 6231–6236, https://doi.org/10.1073/pnas.1713682115.
[22] P. Shao, A.M. Eltony, T.G. Seiler, B. Tavakol, R. Pineda, T. Koller, T. Seiler, S. Yun, Spatially-resolved Brillouin spectroscopy reveals biomechanical abnormalities in mild to advanced keratoconus in vivo, Sci. Rep. 9 (2019) 7467, https://doi.org/10.1038/s41598-019-43811-5.
[23] G. Antonacci, R.M. Pedrigi, A. Kondiboyina, R. de Silva, C. Paterson, R. Krams, P. Török, V.V. Mehta, Quantification of plaque stiffness by Brillouin microscopy in experimental thin cap fibroatheroma, J. R. Soc. Interface 12 (2015) 20150843, https://doi.org/10.1098/rsif.2015.0843.
[24] T. Lainovic, J. Margueritat, Q. Martinet, X. Dagany, L. Blažic, M.D. Rabasovic, A. J. Krmpot, T. Dehoux, Micromechanical imaging of dentin with Brillouin microscopy, Acta Biomater. 105 (2020) 214–222, https://doi.org/10.1016/j.actbio.2020.01.035.
[25] J. Zhang, X.A. Nou, H. Kim, G. Scarcelli, Brillouin flow cytometry for label-free mechanical phenotyping of the nucleus, Lab Chip 17 (2017) 663–670, https://doi.org/10.1039/C6LC01443G.
[26] S. Mattana, M. Mattarelli, L. Urbanelli, K. Sagini, C. Emiliani, M.D. Serra, D. Fioretto, S. Caponi, Non-contact mechanical and chemical analysis of single living cells by microspectroscopic techniques, Light Sci Appl. 7 (2018) 17139, https://doi.org/10.1038/lsa.2017.139.
[27] J. Zhang, F. Alisafaei, M. Nikolić, X.A. Nou, H. Kim, V.B. Shenoy, G. Scarcelli, Nuclear mechanics within intact cells is regulated by cytoskeletal network and internal nanostructures, Small 16 (2020) 1907688, https://doi.org/10.1002/smll.201907688.
[28] S. Pagano, G. Lombardo, S. Caponi, E. Costanzi, A. di Michele, S. Bruscoli, I. Xhimitiku, M. Coniglio, C. Valenti, M. Mattarelli, G. Rossi, S. Cianetti, L. Marinucci, Bio-mechanical characterization of a CAD/CAM PMMA resin for digital removable prostheses, Dent. Mater. 37 (2021) e118–e130, https://doi.org/10.1016/j.dental.2020.11.003.
[29] M. Bailey, M. Alunni-Cardinali, N. Correa, S. Caponi, T. Holsgrove, H. Barr, N. Stone, C.P. Winlove, D. Fioretto, F. Palombo, Viscoelastic properties of biopolymer hydrogels determined by Brillouin spectroscopy: a probe of tissue micromechanics, Sci. Adv. 6 (2020), eabc1937, https://doi.org/10.1126/sciadv.abc1937.
[30] R. Mercatelli, S. Mattana, L. Capozzoli, F. Ratto, F. Rossi, R. Pini, D. Fioretto, F. S. Pavone, S. Caponi, R. Cicchi, Morpho-mechanics of human collagen superstructures revealed by all-optical correlative micro-spectroscopies, Commun Biol. 2 (2019) 117, https://doi.org/10.1038/s42003-019-0357-y.
[31] M. Alunni Cardinali, A. di Michele, M. Mattarelli, S. Caponi, M. Govoni, D. Dallari, S. Brogini, F. Masia, P. Borri, W. Langbein, F. Palombo, A. Morresi, D. Fioretto, Brillouin-Raman microspectroscopy for the morpho-mechanical imaging of human lamellar bone, J. R. Soc. Interface 19 (2022), 20210642, https://doi.org/10.1098/rsif.2021.0642.
[32] C.J. Chan, C. Bevilacqua, R. Prevedel, Mechanical mapping of mammalian follicle development using Brillouin microscopy, Commun. Biol. 4 (2021) 1133, https://doi.org/10.1038/s42003-021-02662-5.
[33] M. Mattarelli, G. Capponi, A.A. Passeri, D. Fioretto, S. Caponi, Disentanglement of multiple scattering contribution in Brillouin microscopy, ACS Photonics 9 (2022) 2087–2091, https://doi.org/10.1021/acsphotonics.2c00322.
[34] I. Remer, R. Shaashoua, N. Shemesh, A. Ben-Zvi, A. Bilenca, High-sensitivity and high-specificity biomechanical imaging by stimulated Brillouin scattering microscopy, Nat. Methods 17 (2020) 913–916, https://doi.org/10.1038/s41592-020-0882-0.
[35] J. Zhang, A. Fiore, S. Yun, H. Kim, G. Scarcelli, Line-scanning Brillouin microscopy for rapid non-invasive mechanical imaging, Sci. Rep. 6 (2016) 35398, https://doi.org/10.1038/srep35398.
[36] B. Krug, N. Koukourakis, J.W. Czarske, Impulsive stimulated Brillouin microscopy for non-contact, fast mechanical investigations of hydrogels, Opt. Express 27 (2019) 26910, https://doi.org/10.1364/oe.27.026910.
[37] G. Scarcelli, S.H. Yun, Confocal Brillouin microscopy for three-dimensional mechanical imaging, Nat. Photonics 2 (2008) 39–43, https://doi.org/10.1038/nphoton.2007.250.
[38] G. Antonacci, V. de Turris, A. Rosa, G. Ruocco, Background-deflection Brillouin microscopy reveals altered biomechanics of intracellular stress granules by ALS protein FUS, Commun. Biol. 1 (2018) 139, https://doi.org/10.1038/s42003-018-0148-x.
[39] K. Elsayad, S. Werner, M. Gallemi, J. Kong, E.R. Sanchez Guajardo, L. Zhang, Y. Jaillais, T. Greb, Y. Belkhadir, Mapping the subcellular mechanical properties of live cells in tissues with fluorescence emission-Brillouin imaging, Sci. Signal. 9 (2016) rs5, https://doi.org/10.1126/scisignal.aaf6326.
[40] F. Scarponi, S. Mattana, S. Corezzi, S. Caponi, L. Comez, P. Sassi, A. Morresi, M. Paolantoni, L. Urbanelli, C. Emiliani, L. Roscini, L. Corte, G. Cardinali, F. Palombo, J.R. Sandercock, D. Fioretto, High-performance versatile setup for simultaneous Brillouin-Raman microspectroscopy, Phys. Rev. X 7 (2017), 031015, https://doi.org/10.1103/PhysRevX.7.031015.
[41] A.J. Traverso, J.V. Thompson, Z.A. Steelman, Z. Meng, M.O. Scully, V.V. Yakovlev, Dual Raman-Brillouin microscope for chemical and mechanical characterization and imaging, Anal Chem. 87 (2015) 7519–7523, https://doi.org/10.1021/acs.analchem.5b02104.
[42] M. Mattarelli, M. Vassalli, S. Caponi, Relevant length scales in Brillouin imaging of biomaterials: the interplay between phonons propagation and light focalization, ACS Photonics 7 (2020) 2319–2328, https://doi.org/10.1021/acsphotonics.0c00801.
[43] S. Caponi, D. Fioretto, M. Mattarelli, On the actual spatial resolution of Brillouin imaging, Opt. Lett. 45 (2020) 1063, https://doi.org/10.1364/OL.385072.
[44] M.A. Cardinali, M. Govoni, D. Dallari, S. Caponi, D. Fioretto, A. Morresi, Mechano-chemistry of human femoral diaphysis revealed by correlative Brillouin-Raman microspectroscopy, Sci. Rep. 10 (2020) 1–11, https://doi.org/10.1038/s41598-020-74330-3.
[45] C.B. Walsh, E.I. Franses, Ultrathin PMMA films spin-coated from toluene solutions, Thin Solid Films 429 (2003) 71–76, https://doi.org/10.1016/S0040-6090(03)00031-2.
[46] H. Richter, Z.P. Wang, L. Ley, The one phonon Raman spectrum in microcrystalline silicon, Solid State Commun. 39 (1981) 625–629, https://doi.org/10.1016/0038-1098(81)90337-9.
[47] X. Zhang, R. Sooryakumar, K. Bussmann, Confinement and transverse standing acoustic resonances in free-standing membranes, Phys. Rev. B Condens. Matter. Mater. Phys. 68 (2003), 115430, https://doi.org/10.1103/PhysRevB.68.115430.
[48] J.R. Sandercock, Structure in the Brillouin spectra of thin films, Phys. Rev. Lett. 29 (1972) 1735–1738, https://doi.org/10.1103/PhysRevLett.29.1735.
[49] O. el Abouti, J. Cuffe, E.H. el Boudouti, C.M. Sotomayor Torres, E. Chavez-Angel, B. Djafari-Rouhani, F. Alzina, Comparison of Brillouin light scattering and density of states in a supported layerAnalytical and Experimental Study, Crystals (Basel) 12 (2022) 1212, https://doi.org/10.3390/cryst12091212.
[50] N. Gomopoulos, W. Cheng, M. Efremov, P.F. Nealey, G. Fytas, Out-of-plane longitudinal elastic modulus of supported polymer thin films, Macromolecules 42 (2009) 7164–7167, https://doi.org/10.1021/ma901246y.
[51] J.R. Sandercock, Trends in Brillouin scattering: studies of opaque materials, supported films, and central modes, in: M. Cardona (Ed.), Light Scattering in Solids III 51, Springer, Berlin Heidelberg, 1982, pp. 173–206, https://doi.org/10.1007/3540115137_6.
[52] X. Zhang, R. Sooryakumar, A.G. Every, M.H. Manghnani, Observation of organ-pipe acoustic excitations in supported thin films, Phys. Rev. B 64 (2001), 081402, https://doi.org/10.1103/PhysRevB.64.081402.
[53] V. Bonal, J.A. Quintana, J.M. Villalvilla, R. Muñoz-Mármol, J.C. Mira-Martínez, P. G. Boj, M.E. Cruz, Y. Castro, M.A. Díaz-García, Simultaneous determination of refractive index and thickness of submicron optical polymer films from transmission spectra, Polymers (Basel) 13 (2021) 2545, https://doi.org/10.3390/polym13152545.
[54] D. Schneider, P.J. Beltramo, M. Mattarelli, P. Pfleiderer, J. Vermant, D. Crespy, M. Montagna, E.M. Furst, G. Fytas, Elongated polystyrene spheres as resonant building blocks in anisotropic colloidal crystals, Soft Matter 9 (2013) 9129, https://doi.org/10.1039/c3sm50959a.
[55] N. Ismail, C.C. Kores, D. Geskus, M. Pollnau, Fabry-Pérot resonator: spectral line shapes, generic and related airy distributions, linewidths, finesses, and performance at low or frequency-dependent reflectivity, Opt. Express 24 (2016) 16366, https://doi.org/10.1364/OE.24.016366.
[56] M. Lelek, M.T. Gyparaki, G. Beliu, F. Schueder, J. Griffié, S. Manley, R. Jungmann, M. Sauer, M. Lakadamyali, C. Zimmer, Single-molecule localization microscopy, Nat. Rev. Methods Primers 1 (2021) 39, https://doi.org/10.1038/s43586-021-00038-x.
[57] R.J. Smith, F. Pérez-Cota, L. Marques, M. Clark, 3D phonon microscopy with sub-micron axial-resolution, Sci. Rep. 11 (2021) 3301, https://doi.org/10.1038/s41598-021-82639-w.